

Gravitational Lensing by Galaxy Groups in the Hubble Deep Field

David C. Fox

Physics Department, Harvard University, Jefferson Physical Laboratories, Cambridge, MA 02138

`dcfox@cfa.harvard.edu`

and

Ue-Li Pen

Canadian Institute for Theoretical Astrophysics, University of Toronto, McLennan Labs, 60 St. George Street, Toronto, ON, M5S 3H8, Canada

`pen@cita.utoronto.ca`

ABSTRACT

We investigate strong lensing of galaxies in the Hubble Deep Field by foreground groups and clusters of galaxies with masses from 10^{13} to $10^{15} M_{\odot}$. Over this mass range, groups with the profile of Navarro, Frenk, & White (1995) are less efficient than singular isothermal spheres at producing multiple images of galaxies, by factors of 5×10^{-2} to 10^{-3} . This difference highlights the sensitivity of the lensing cross section to the central density profile. Nonetheless, with either profile we find that the expected number of galaxies lensed by groups in the Hubble Deep Field is at most $\lesssim 1$, consistent with the lack of clearly identified group lens systems.

Subject headings: dark matter — galaxies: clusters : general — gravitational lensing

1. INTRODUCTION

Navarro, Frenk, & White (1995) investigated the structure of clusters of galaxies in N -body simulations of the Standard Cold Dark Matter cosmology. From the virial radius, r_{vir} ,

down to $0.01r_{\text{vir}}$, they found that the dark matter profiles of equilibrium clusters followed the form

$$\rho(r) \propto (r/r_s)^{-1}(1 + r/r_s)^{-2} \quad (1)$$

characterized by a single scale, r_s . The NFW profile has a central density cusp, ($\rho \propto r^{-1}$), shallower than the singular isothermal sphere ($\rho \propto r^{-2}$), but gradually turns over and becomes steeper ($\propto r^{-3}$) at large radii. Dubinski & Carlberg (1991) had earlier found both features in higher resolution simulations of galaxies, which they fit with a Hernquist (1990) profile,

$$\rho(r) \propto (r/r_s)^{-1}(1 + r/r_s)^{-3}. \quad (2)$$

Navarro, Frenk, & White (1996) found that the density profiles of equilibrium dark matter halos spanning a mass range from dwarf galaxies ($3 \times 10^{11} M_{\odot}$) to rich clusters ($3 \times 10^{15} M_{\odot}$) could be described by equation (1). They suggested that this profile was a universal form for dark matter halos. Navarro, Frenk, & White (1997) found that the NFW profile also fit simulated halos for a variety of CDM cosmologies. Other numerical simulations (e.g., Cole & Lacey 1996; Brainerd, Goldberg, Villumsen 1998) have generally agreed with the NFW profile. However, higher resolution simulations (Tormen, Bouchet, & White 1997; Fukushige & Makino 1997) have suggested somewhat steeper central slopes, though still shallower than the singular isothermal sphere. In the highest resolution simulations (Moore et al. 1998, 1999), the central density profile is $\propto r^{-p}$ with $p = 1.4\text{--}1.5$.

It is important to test the predicted universal form of dark matter halos through observations. There have been a number of tests on cluster scales. Bartelmann (1996) showed that gravitational lenses with the NFW form could produce the radial arcs seen in some clusters, but noted that the narrowness of observed tangential arcs might pose a problem. Williams, Navarro, & Bartelmann (1999) found that both the radii and width of tangential arcs could only be reconciled with the NFW profile if clusters with low velocity dispersion ($\sim 1000 \text{ km sec}^{-1}$) had massive ($\sim 3 \times 10^{12} h^{-1} M_{\odot}$) central galaxies, increasing the slope of the central density profile. Observations of galaxy number density profiles (Carlberg et al. 1997), and X-ray surface brightness and temperature profiles (Markevitch et al. 1999; Nevalainen, Markevitch, & Forman 1999) seem generally consistent with the NFW profile. On somewhat smaller mass scales, Mahdavi et al. (1999) studied a sample of 20 galaxy groups, and concluded that the NFW profile successfully reproduced their X-ray emission and the density and velocity distributions of their galaxies. On the other hand, the measured rotation curves of dwarf spiral galaxies imply constant density cores which are inconsistent with the Hernquist, NFW, and singular isothermal sphere profiles (Moore et al. 1994; Flores & Primack 1994; Burkert 1995). Similar results have been found for low surface brightness galaxies (Kravtsov et al. 1998; Moore et al. 1999). Since observational limits on the gas and

stellar masses indicate that these galaxies are dominated by dark matter, these results pose a serious challenge to the universality of the NFW profile. Ejection of baryons by supernova explosions might lead to formation of a flat core (Navarro, Eke, & Frenk 1996; Gelato & Sommer-Larsen 1999), although this suggestion has been criticized as unrealistic (Burkert & Silk 1997), especially in the more massive low surface brightness galaxies (Kravtsov et al. 1998; Moore et al. 1999). Kravtsov et al. (1998) find that profiles with a shallow cusp, $\rho(r) \propto r^{-0.2}$, fit both the observations and their simulations. However, higher resolution simulations have not confirmed the simulations, instead showing a steep divergence, $\rho(r) \propto r^{-1.5}$ (Moore et al. 1999).

Both simulations and observations highlight the need for tests of the NFW profile over a wide range of masses and radii. Some tests, such as strong lensing by clusters, are very sensitive to the mass profile at small radii, $r \ll r_s$. Others, such as the X-ray temperature profiles reported to date, are limited by finite spatial resolution, and are more useful as probes at intermediate and large radii.

We propose another test of the NFW profile at small radii: statistics of gravitational lensing by groups. The dramatic images of lensed arcs observed in clusters are familiar (e.g., Kneib et al. 1996). Groups are less massive than clusters and thus have smaller lensing cross sections. However, clusters are rare objects, making up a small fraction of the matter in the universe, while groups are much more numerous. Others have considered lensing of quasars by groups and clusters (Narayan & White 1988; Kochanek 1995; Flores & Primack 1996; Maoz et al. 1997; Keeton 1998). Cooray (1999) has made predictions of the number of arcs on the whole sky, but has restricted his attention to clusters with mass $M \geq 7.5 \times 10^{14} M_\odot$, modeled as singular isothermal spheres. Barkana & Loeb (2000) have estimated the probability of lensing of galaxies observable with the Next Generation Space Telescope by singular isothermal spheres of galaxy mass and higher.

Keeton (1998), noting that the NFW profile has a smaller lensing cross section than the singular isothermal sphere, particularly at lower masses, has suggested that this lower cross section may explain the lack of observations of giant arcs in groups as compared to clusters. We will see that the difference in cross sections is due to the difference between the two profiles at small radii. This sensitivity to the inner part of the density profile makes the statistics of lensing by groups a potential test of the inner portions of the NFW profile in groups. By calculating lensing rates for both the NFW and SIS models, we hope to span the range of central profiles seen in simulations.

We consider the Hubble Deep Field as a tool for studying lensing by groups. The Hubble Deep Field (HDF) provides high-resolution images and photometry taken by the Hubble Space Telescope in four spectral bands, F300W, F450W, F606W, and F814W (each

labeled according to the approximate wavelength in nm of the peak spectral sensitivity of its filter). The photometry extends to 10σ limits of 27 to 28 in the AB magnitude system (see, e.g., Fukugita et al. 1996), one to three magnitudes deeper than current ground-based images (Williams et al. 1996). This depth allows detection of a large number of ordinary galaxies at redshifts > 1 . Early estimates of the optical depth for lensing at these redshifts suggested that the Hubble Deep Field should contain between three and 10 gravitationally lensed galaxies with multiple images (Hogg et al. 1996).

Several groups have identified possible lens systems in the HDF on the basis of morphologies and colors. Hogg et al. (1996) have applied a semi-automated technique based on the CLASS survey (e.g., Myers et al. 1995) to identify lens candidates. They cite a system with an arc $1.8''$ from an elliptical galaxy, and a possible counter image $1.4''$ on the opposite side, as the most likely of the 24 candidates examined so far, and also mention another elliptical and arc separated by $0.9''$ (but without a counter image). Zepf, Moustakas, & Davis (1997) identified three candidates by visual inspection, including a system of four blue galaxies separated by $\lesssim 1.0''$, as well as the two systems mentioned by Hogg et al. (1996). However, subsequent spectroscopy with the Low-Resolution Imaging Spectrograph on the Keck telescope ruled out the first two candidate systems and provided inconclusive evidence on the third. This led Zepf et al. (1997) to conclude that there might be no more than one multiply-imaged galaxy in the HDF down to an AB magnitude of 27 in F814W, similar to the magnitude of the candidates examined. Cooray, Quashnock, & Miller (1999) calculated the number of multiply-imaged galaxies expected due to lensing by galaxies, modeled as singular isothermal spheres, and have used the paucity of apparent lensed galaxies to place a lower limit on the difference, $\Omega_0 - \Lambda$, between the matter density in the universe, $\Omega_0 \equiv \rho_0/\rho_c$, and the cosmological constant, Λ .

Since foreground galaxies and groups of galaxies can both contribute to lensing of background galaxies, the actual number of lensed galaxies would be an upper limit on each contribution. Even allowing for the possibility of failure to identify some lensed galaxies, this upper limit appears likely to be quite low. We want to know if such a limit can distinguish between NFW and the singular isothermal sphere density profiles for groups. We therefore calculate the number of galaxies in the Hubble Deep Field expected to have multiple images due to lensing by groups (and clusters) of either profile. In §2, we describe the details of our calculation and our underlying assumptions. We present the results in §3, and discuss how they depend on the choice of lens profile and cosmology in §4. In §5, we summarize our conclusions and prospects for future work.

2. FINDING THE NUMBER OF LENSED GALAXIES

We discuss the basic elements which determine the lensing probability: the cosmology, the lens population, and the source galaxy redshifts. Finally, we combine these elements to find the number of galaxies in the Hubble Deep Field expected to have multiple images.

2.1. Cosmologies

We consider three different basic cosmologies: a Standard CDM model with $\Omega_0 = 1$ (SCDM), a low-density open model with $\Omega_0 = 0.3$ (OCDM), and a flat model with $\Omega_0 = 0.3$ and $\Lambda = 0.7$ (Λ CDM). In all three cases, we assume a Hubble constant, $H_0 = 70$ km/sec/Mpc ($h = 0.7$) and a baryon density of $\Omega_b h^2 = 0.019$ inferred from big bang nucleosynthesis and the deuterium abundance in quasar absorption line systems (Burles & Tytler 1998).

2.2. The Lens Population

We discuss the abundance of groups and clusters, their density profiles, and the cross section of an individual lens. We are primarily interested in groups, since they are more numerous. However, given the universal NFW form of dark matter halos found in simulations, we treat both groups and clusters as halos in a continuum in mass.

2.2.1. Mass Function

We calculate the abundance of halos as a function of mass, or mass function, using the method of Press & Schechter (1974). At early times, the universe is homogeneous with only small density perturbations $\delta \equiv (\rho - \bar{\rho})/\bar{\rho} \ll 1$ with respect to the mean density, $\bar{\rho}(z) = \rho_0(1 + z)^3$. The Press-Schechter method relates these density perturbations at large z , where their evolution can be described by linear theory, to the highly nonlinear ($\delta \approx 200$) collapsed structures at low redshifts. Despite its simplifying assumptions, the Press-Schechter method reproduces the mass function found in simulations (Eke, Cole, & Frenk 1996).

The Press-Schechter method is based on the spherical model for collapse of a homogeneous perturbation, known as the spherical top-hat model. Such a perturbation is unaffected by the isotropic universe outside, so it behaves as a Friedmann universe of its own with mean density ρ' and expansion rate H' . A sufficiently dense perturbation will be bound, and will turn around after a finite time, t_{ta} . Without pressure support, the perturbation would col-

lapse to infinite density in a collapse time $t_c = 2t_{\text{ta}}$. Due to pressure, the perturbation is instead assumed to reach virial equilibrium by the same time, t_c .

We are interested in the abundance of virialized halos at a given redshift, z . For a given cosmology, the collapse time of a spherical perturbation depends on its overdensity, with the densest perturbations collapsing first. At early times, when the overdensity of the perturbation, $\delta' \equiv (\rho' - \bar{\rho})/\bar{\rho}$ is much less than 1, its evolution can be described by linear perturbation theory. While the spherical model describes the nonlinear evolution of δ' , perturbations can still be characterized by the extrapolation δ'_0 of $\delta'(z)$ to $z = 0$ in linear theory. In the spherical model, perturbations for which δ'_0 exceeds a threshold $\delta_c(z)$ will virialize at redshift z . Thus, $\delta_c(z)$ relates the overdensity in linear theory to the highly nonlinear collapse. For the $\Lambda = 0$ case, $\delta_c(z)$ can be obtained analytically in terms of the age of universe, $t(z)$, and Ω_0 (Kochanek 1995). For the ΛCDM case, we calculate its inverse, $z_c(\delta_c)$, (Eke et al. 1996) and solve for δ_c numerically.

Of course, the universe doesn't consist of a single homogeneous spherical perturbation. It is characterized by the overdensity field $\delta(\mathbf{r}, z)$, where \mathbf{r} is the position in a co-moving coordinate system such that $d\mathbf{r}/dt = 0$ corresponds to unperturbed Hubble flow. The Press-Schechter model assumes that $\delta(\mathbf{r}, z)$ is a Gaussian random field at large z . Its Fourier components, $\delta_{\mathbf{k}}(z)$ are therefore uncorrelated and drawn from Gaussian distributions with variance $\langle |\delta_{\mathbf{k}}|^2 \rangle$.

To connect this picture to the spherical collapse model, we smooth $\delta(\mathbf{r}, z)$ using a spherical top-hat window function of co-moving radius R , or a physical radius of $R/(1+z)$, corresponding to a mass scale $M = 4\pi\rho_0 R^3/3$. The Press-Schechter method assumes that matter at \mathbf{r} will become part of a halo of mass M at redshift z , provided that M is the largest mass scale for which the smoothed overdensity at \mathbf{r} exceeds the threshold from the spherical model.

The mean overdensity, $(\delta M/M)(R)$, within a sphere of co-moving radius R will also have a Gaussian distribution, so the probability of $\delta M/M$ exceeding δ_c is readily calculated. The variance, σ_R^2 or $\sigma^2(M)$, of the $\delta M/M$ distribution, is related to the power spectrum, $P(k) \equiv \langle |\delta_{\mathbf{k}}|^2 \rangle$, by

$$\sigma^2(M) = \sigma_R^2 = (2\pi)^{-3} \int_0^\infty 4\pi k^2 dk \langle |\delta_{\mathbf{k}}|^2 \rangle W^2(kR) \quad (3)$$

where

$$W(u) \equiv 3 \left(\frac{\sin u - u \cos u}{u^3} \right). \quad (4)$$

The probability that a given spherical region will collapse depends on the ratio of σ_R to $\delta_c(z)$. Thus, we must also extrapolate σ_R to $z = 0$ in linear theory by extrapolating the

power spectrum in equation (3). Ignoring factors independent of k and z , the evolution of $P(k, z)$ is

$$P(k, z) \propto P(k, z_i) T^2(k, z) D_1^2(z) \quad (5)$$

where $D_1(z)$ is the linear growth function, and $T(k, z)$, which describes the scale-dependent evolution, is called the transfer function. We assume a scale-invariant primordial power spectrum $P(k, z_i) \propto k$ at high redshift z_i . We use a BBKS (Bardeen et al. 1986) transfer function with the shape parameter, Γ_{eff} , defined by

$$\Gamma_{\text{eff}} = \Omega_0 h \exp \left(\frac{-\Omega_b(\Omega_0 + 1)}{\Omega_0} \right), \quad (6)$$

of 0.18 for $\Omega_0 = 0.3$ and 0.65 for $\Omega_0 = 1$. We also consider an $\Omega_0 = 1$ model with a lower value of 0.25 for Γ . We normalize the power spectrum by fixing σ_R on a scale of $R = 8 h^{-1} \text{Mpc}$. For each cosmology, the value of σ_8 is chosen to reproduce the observed abundance of clusters as a function of their X-ray temperature (Pen 1998), yielding $\sigma_8 = 0.53, 0.91$, and 1.0 for SCDM, OCDM, and Λ CDM, respectively.

Finally, the number of halos per co-moving volume, $dn/dM(M, z)$, as a function of the virial mass, M , and the redshift, z is

$$\frac{dn}{dM}(M, z) = -\frac{1}{\sqrt{2\pi}} \frac{\rho_0}{M} \frac{\delta_c(z)}{\sigma(M)} \frac{\partial \ln \sigma^2(M)}{\partial M} \exp \left(-\frac{\delta_c^2(z)}{2\sigma^2(M)} \right). \quad (7)$$

The resulting mass functions are shown in Figure 1 for redshifts of 0 and 0.6. We consider groups and clusters by restricting our attention to the mass range from 10^{13} to $10^{15} M_\odot$. We will see that the number of lensed galaxies predicted is not sensitive to the upper limit of this range, because of the exponential cutoff in the mass function for $\sigma^2(M) < \delta_c^2$. The lower limit on the mass will have a significant effect only for the singular isothermal sphere.

2.2.2. Density Profiles

We consider two choices for the density profiles of the lens halos, a singular isothermal sphere (SIS) with

$$\rho(r) = \frac{\sigma_v^2}{2\pi G r^2} \quad (8)$$

characterized by a one-dimensional velocity dispersion, σ_v^2 , and a profile of the form found by Navarro et al. (1997) with

$$\rho(r) = \frac{\rho_s}{(r/r_s)(1+r/r_s)^2} \quad (9)$$

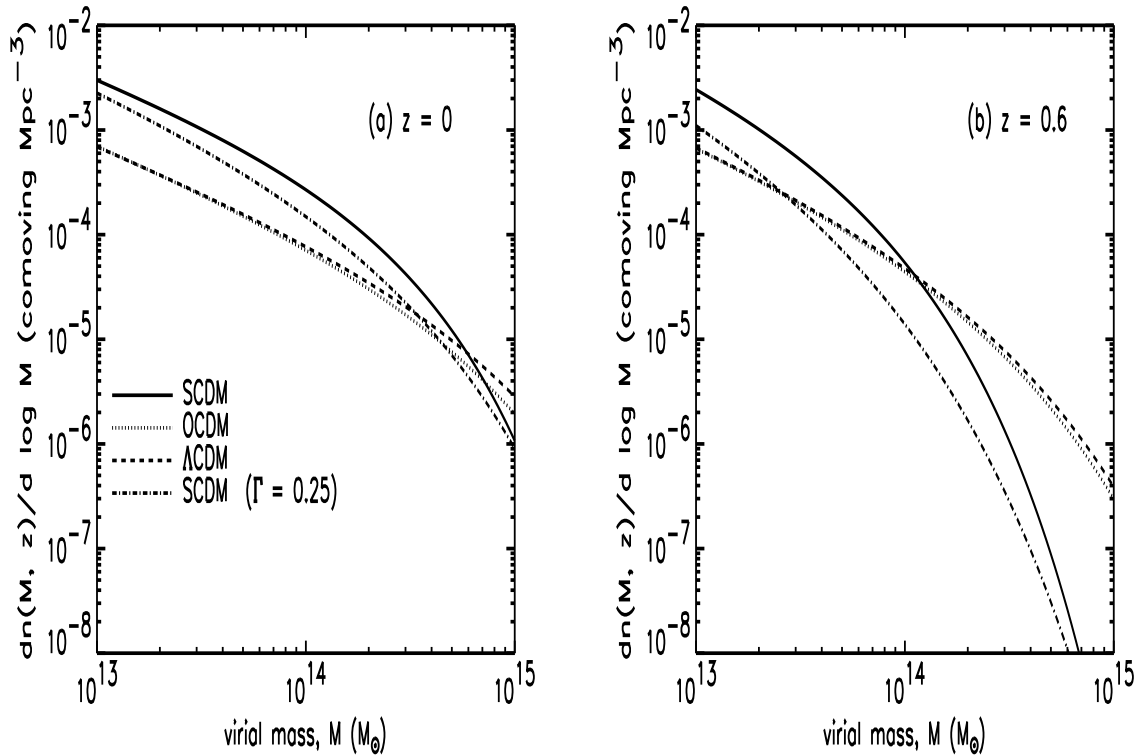


Fig. 1.— Press-Schechter mass function for (a) $z = 0$ and (b) $z = 0.6$ for our three basic cosmologies, Standard CDM (solid line), Open CDM with $\Omega = 0.3$ (dotted line), and Λ CDM with $\Omega = 0.3$, $\Lambda = 0.7$ (dashed line), as well as a fourth SCDM variant with $\Omega = 1$ but $\Gamma = 0.25$ (dot-dashed line). The power spectrum has been normalized using the temperature function of clusters to fix σ_8 of 0.53, 0.91, and 1.0 for the SCDM (and variant), OCDM, and Λ CDM cases, respectively.

characterized by a scale radius, r_s , and normalization, $\rho_s = \delta_{\text{NFW}}\rho_c(z)$, where $\rho_c(z)$ is the critical density at redshift z , and we use δ_{NFW} instead of δ_c to avoid confusion with the overdensity for spherical collapse.

Our Press-Schechter mass function gives, for each redshift, the co-moving number density of halos, $dn/dM(M, z) dM$, with virial mass between M and $M + dM$. We need to fix the free parameters of the density profile in terms of M and z . One constraint is simply that the profile have the correct virial mass. In the spherical top-hat collapse model, the density at virialization, $\rho_{\text{vir}} \equiv \eta_{\text{vir}}\bar{\rho}(z)$, can be calculated using the virial theorem and conservation of energy. It depends only on the redshift, z , and on the cosmology (see Eke et al. (1996) for the Λ CDM case). The virial radius, r_{vir} , is fixed by $M_{\text{vir}} \equiv 4\pi\bar{\rho}\eta_{\text{vir}}r_{\text{vir}}^3/3$. Then we can write the virial mass condition as

$$\frac{3M(r)}{4\pi r^3} \Big|_{r=r_{\text{vir}}} = \rho_{\text{vir}} = \eta_{\text{vir}}\bar{\rho}(z). \quad (10)$$

For the singular isothermal sphere, this condition is sufficient to fix the one free parameter, σ_v^2 . For the NFW profile, however, we need additional information. Navarro et al. (1997) have investigated the relationship between the normalization, δ_{NFW} , and the mass M_{200} within a radius r_{200} containing a mean density of 200 times the critical density $\rho_c(z)$. For a wide variety of cosmologies, they find that δ_{NFW} and M_{200} are well correlated. While the precise relation depends on cosmology, it can be fit by

$$\delta_{\text{NFW}}(M_{200}, z) = 3 \times 10^3 \Omega(z) \left(\frac{1 + z_{\text{form}}}{1 + z} \right)^3 \quad (11)$$

where the formation redshift, z_{form} , is defined as the redshift by which a fraction $f = 10^{-2}$ of the halo mass has accumulated, according to Press-Schechter formalism of Lacey & Cole (1993). This redshift is given implicitly in terms of the error function, erfc , by

$$\frac{\delta_c(z_{\text{form}}) - \delta_c(z)}{\sqrt{2[\sigma^2(fM_{200}) - \sigma^2(M_{200})]}} = \text{erfc}^{-1}\left(\frac{1}{2}\right), \quad (12)$$

where $\sigma^2(M)$ is the variance of the fractional mass fluctuations on mass scale M in the spherical top hat model, defined in §2.2.1. For $f \ll 1$, this simplifies to

$$\delta_c(z_{\text{form}}) = \delta_c(z) + C'\sigma(fM_{200}) \quad (13)$$

where $C' = \sqrt{2}\text{erfc}^{-1}(1/2) \approx 0.67$.

Note that while Navarro et al. (1997) referred to M_{200} as the virial mass and r_{200} as the virial radius, the overdensity with respect to the critical density $\rho_c(z_{\text{vir}})$ at virialization

is only equal to 200 for Standard CDM. Unfortunately, the relation between M_{200} and M_{vir} depends on the normalization δ_{NFW} of the profile. We initially approximate M_{200} by M in solving equation (13) for δ_{NFW} . Given δ_{NFW} , we can solve equation (10) for the remaining free parameter, r_s . We then use δ_{NFW} and r_s to find a new approximation for M_{200} , and repeat. This procedure converges rapidly, with only a few percent change in the parameters on the first iteration, and tenths of a percent thereafter.

2.2.3. Properties of the Lenses

For each density profile, we find the projected surface mass density, Σ , as a function of the projected radius from the center of the lens. The lens properties are determined by the convergence, $\kappa = \Sigma/\Sigma_{\text{cr}}$, where

$$\Sigma_{\text{cr}} = \frac{c^2}{4\pi G} \frac{D_s}{D_l D_{ls}}, \quad (14)$$

and D_s , D_l , and D_{ls} are angular diameter distances to the source, to the lens, and from the lens to the source, respectively. For the Λ CDM case, we calculate the angular diameter distances according to Carroll, Press, & Turner (1992).

Following Schneider, Ehlers, & Falco (1992), it is convenient to choose an arbitrary length scale ξ_0 in the image plane, and a corresponding scale $\eta_0 = (D_s/D_l)\xi_0$ in the source plane. In units of these length scales, the source position, \mathbf{y} , and the image position, \mathbf{x} , are related by the lens equation,

$$\mathbf{y} = \mathbf{x} - \nabla\psi(\mathbf{x}), \quad (15)$$

where the lens potential, ψ , satisfies a Poisson equation $\nabla^2\psi = 2\kappa$. For an axisymmetric lens, ψ depends only on radius, and the source, lens, and image positions are collinear. Using the divergence theorem, equation (15) simplifies to the one-dimensional form

$$y = x - \frac{m(x)}{x}, \quad (16)$$

where x and y are both signed quantities, and

$$m(x) \equiv 2 \int_0^{|x|} dx' x' \kappa(x') \quad (17)$$

is the dimensionless mass inside a cylinder of dimensionless radius $|x|$.

When comparing different profiles, we must use dimensional quantities. The dimensional source position, $\eta \equiv \eta_0 y$, and image positions, $\xi \equiv \xi_0 x$, are related by

$$\eta = \frac{D_s}{D_l} \xi \left[1 - \frac{M_{\text{cyl}}(\xi)}{\pi \Sigma_{\text{cr}} \xi^2} \right] \quad (18)$$

$$= \frac{D_s}{D_l} \xi \left[1 - \frac{\bar{\Sigma}(\xi)}{\Sigma_{\text{cr}}} \right]. \quad (19)$$

where $M_{\text{cyl}}(\xi)$ is the mass within a cylinder of radius $|\xi|$, and $\bar{\Sigma}(\xi) \equiv M_{\text{cyl}}(\xi)/\pi\xi^2$ is the mean surface density within the cylinder.

Figure 2 shows the lens equation (19) for NFW and SIS profiles of the same mass and lens and source redshifts. The particular choice of mass and redshifts, explained in §4.1, is unimportant here. A point source at a particular position η_p relative to the center of the lens will have an image at each ξ where $\eta(\xi) = \eta_p$. The cross section for multiple imaging is simply the area of the region of the source plane for which the lens equation has multiple solutions.

At locations in the source plane where $d\eta/d\xi = 0$, so that $\eta(\xi)$ is tangent to the horizontal, the number of images changes by two. Such locations are called radial caustics and the corresponding curves in the image plane are called radial critical curves. If the surface density, Σ , decreases with radius, the slope $d\eta/d\xi$ is monotonic increasing with $\xi > 0$. Thus, there is a single caustic radius, $\eta_c = \eta_0 y_c$, where the number of images changes from one to three. Outside this caustic radius, there is no multiple imaging. When the source is centered on the lens, so $\eta = 0$, the two outer images merge to form an Einstein ring. The radial critical curve is always inside the Einstein ring radius, for Σ monotonic decreasing. The singular isothermal sphere is a special case, because $m(x)/x$ is constant and does not go to 0 at $x = 0$. As a result, it has no radial caustic and its central image is suppressed.

For the singular isothermal sphere, which has no intrinsic length scale, we make the usual choice of $\xi_0 = 4\pi(\sigma_v/c)^2 D_l D_{ls}/D_s$, set by the ratio of the mass normalization to the critical density. Then $\kappa(x) = 1/2x$ and $m(x) = |x|$. It is easy to show that the lens equation has two image position solutions when $|y| \leq 1$, so the cross section is $\sigma = \pi\eta_0^2$.

Bartelmann (1996) gives formulas for κ and m of the NFW profile, for ξ_0 chosen equal to the scale radius, r_s . Since the NFW profile has one length scale, and the ratio $\Sigma_{\text{cr}}/\rho_s$ introduces a second, the lens properties no longer scale with ξ_0 the way they do for the singular isothermal sphere. For each lens-source pair, we must solve numerically for the caustic radius, y_c , and cross section, $\sigma = \pi y_c^2 \eta_0^2$, for multiple imaging.

2.3. The Source Galaxies

The lensing cross section depends on the source redshift through the distances $D_s(z_s)$ and $D_{ls}(z_l, z_s)$ in the critical density, Σ_{cr} . Several groups (Lanzetta, Yahil, & Fernández-Soto 1996; Sawicki, Lin, & Yee 1997; Wang, Bahcall, & Turner 1998; Fernández-Soto, Lanzetta, &

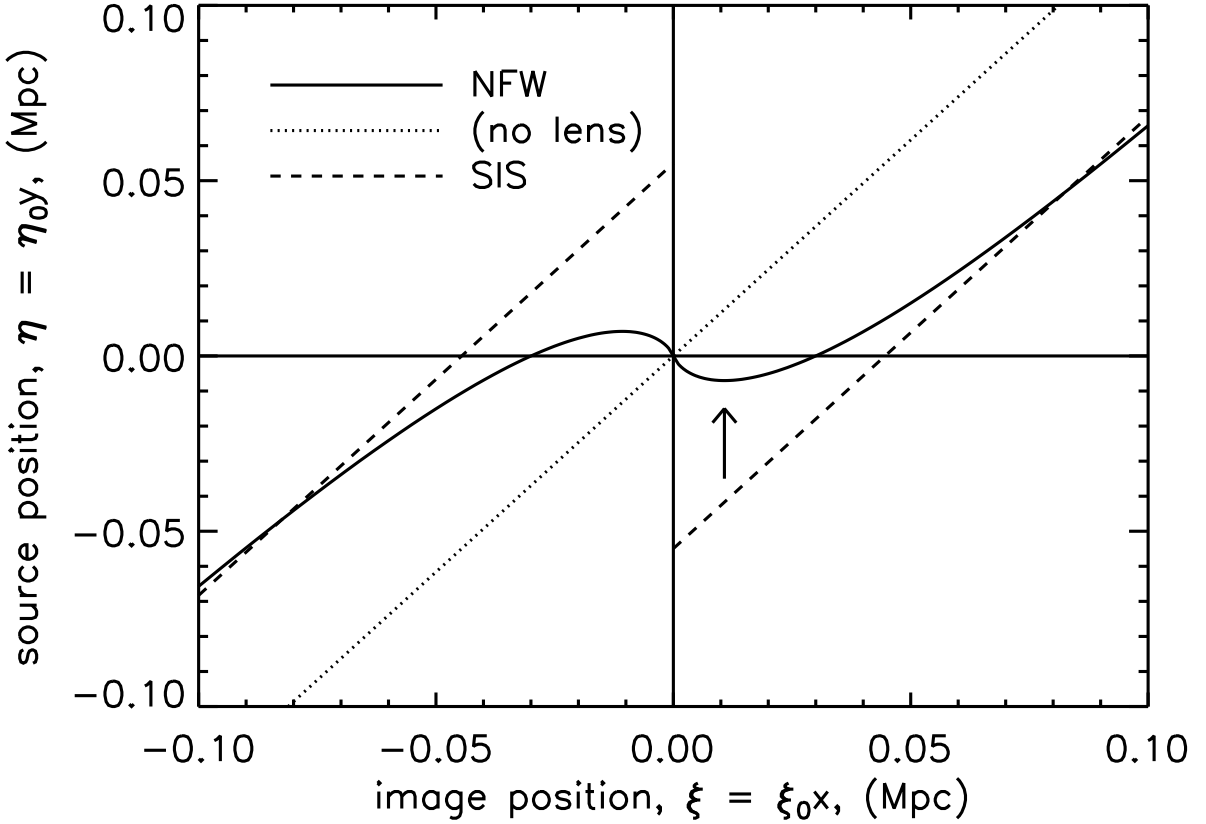


Fig. 2.— Source position, η , as a function of image position, ξ , for NFW (solid) and SIS (dashed) lenses with $M = 2 \times 10^{14} M_\odot$, and $z_l = 0.6$, and a source at redshift $z_s = 3$, in an OCDM cosmology. The diagonal dotted line shows the relation in the absence of any lens. A horizontal line of fixed source position, η , may intersect each curve at multiple image positions, ξ . For the NFW lens, the onset of multiple imaging occurs at a local minimum of $\eta(\xi)$, indicated by the arrow, producing a radial caustic crossing. The SIS profile is sufficiently singular that it has no local minimum, and the radial caustic is suppressed.

Yahil 1999) have obtained photometric redshift estimates for the galaxies in the HDF, with results largely consistent with available spectroscopic redshifts and with each other (Hogg et al. 1998).

We use the Fernández-Soto et al. (1999) catalog of galaxies in the Hubble Deep Field. The selection criteria for this catalog are described in detail in Lanzetta et al. (1996) and Fernández-Soto et al. (1999). In brief, Fernández-Soto et al. (1999) start by identifying sources which exceed a minimum surface brightness threshold in a smooth version of the F814W HDF images. To include low surface brightness galaxies, they choose a threshold $\mu_{AB(8140)} = 26.1 \text{ arcsec}^{-2}$, corresponding to a signal-to-noise ratio of only 1.4 per pixel, but require 10 contiguous pixels above this threshold. This combination of criteria is roughly equivalent to an isophotal magnitude limit of $AB(8140) = 30.6$. To estimate the completeness limit of the sample, they test the sensitivity of the identification procedure to the smoothing length and threshold. They find that the list of objects identified is insensitive to these parameters for $AB(8140) < 28$. Fernández-Soto et al. (1999) therefore restrict their sample to $AB(8140) < 28.0$. Near the edge of the Hubble Deep Field, they impose a stricter magnitude cut of 26.0, citing poorer quality images.

Fernández-Soto et al. (1999) estimate photometric redshifts for the 946 galaxies in the interior and an additional 121 galaxies near the edge meeting these criteria. They supplement the Hubble Space Telescope images with infrared photometry from the observations of Dickinson et al. (1998) to break degeneracies in the photometric redshift estimation. They also include published spectroscopic redshifts for 108 of the sources in the catalog. We use their full catalog of 1067 spectroscopic or photometric redshifts as our source redshift distribution.

2.4. Putting It All Together

We discuss the optical depth for lensing, observational selection effects, magnification bias, and the expected number of multiply-imaged galaxies in the Hubble Deep Field.

2.4.1. Optical Depth and Lensing Probability

The optical depth, τ , for multiple imaging of a source at fixed redshift, z_s , is simply the fraction of the source plane area, $4\pi D_s^2(z_s)$, covered by discs of radius y_c around each lens position. The cross section, σ , of an individual lens is $\sigma_y \eta_0^2 \equiv \pi y_c^2 \eta_0^2$. Multiplying by the

number of groups of mass M and redshift z_l in a co-moving volume $dV_{\text{com}}/dz_l dz_l$, we obtain

$$\begin{aligned} d\tau &= \frac{\sigma_y \eta_0^2}{4\pi D_s^2} \frac{dn}{dM}(M, z) dM \frac{dV_{\text{com}}}{dz_l} dz_l \\ &= \frac{\sigma_y \xi_0^2 (1 + z_l)^2}{H(z_l)} dz_l \frac{dn}{dM}(M, z) dM. \end{aligned} \quad (20)$$

The total optical depth is small, so the lensing probability is equal to $\tau = \int d\tau$.

2.4.2. Number of Lensed Galaxies

We obtain the total number of lensed galaxies expected by multiplying the number distribution of source galaxies $n_{\text{gal}}(z_s) dz_s$ by the lensing probability, τ , and integrating over the source redshift, z_s . Since we are interested in the number of lensed galaxies in the Hubble Deep Field, we can use the delta-function distribution of the discrete catalog of photometric redshifts from Fernández-Soto et al. (1999) directly, without smoothing, changing the normalization, or correcting for redshift clustering.

2.4.3. Observational Selection Effects

The searches for lensed galaxies in the HDF do not explicitly describe criteria for identifying lens candidates. This makes it difficult to estimate their detection efficiency. The best we can do is to try to infer the criteria from the characteristics of the actual candidates selected. The lens candidates are selected on the basis of morphology and color. Specifically, they include two types of systems, those consisting of closely spaced galaxies of similar colors, which might be multiple images of a single source galaxy, and those consisting of a red elliptical accompanied by a blue arc, which might represent a lens galaxy and an image of a lens source respectively (Zepf et al. 1997). We use multiple imaging as a proxy for the latter case as well as the former.

Several observational selection effects might interfere with the detection of multiple imaging, thereby reducing the number of lens systems observed. The point spread function of the HDF images is approximately $0.1''$ in width, so even closely spaced images should be easily resolved. In any case, the typical image separation increases with lens mass, so spatial resolution is less likely to be a problem for detecting lensing by groups, even in ground-based images.

A more likely concern is the possibility that lens systems with widely spaced images might be missed. Even in the two systems identified by Zepf et al. (1997) as multiple

imaging candidates, with separations of $1''$ and $3''$, spectroscopy showed that the putative multiple images were actually different galaxies. The search for lens candidates may have been limited, explicitly or implicitly, to small separations, since such false-positive cases would be more likely at larger separations.

The description of a red elliptical as a possible lens galaxy suggests that the searches may have focused on lensing by galaxies. However, since groups contain galaxies, this might not be a serious bias.

Again, without quantitative criteria, it is difficult to estimate the reduction in detection efficiency due to such factors. We therefore calculate the total number of multiply-imaged galaxies, keeping in mind that the number actually observed may be lower.

2.4.4. *Magnification Bias*

Another related concern is magnification bias. Lens magnification increases the angular area of an image, while leaving its surface brightness unchanged, thereby increasing the flux. If the search for lensed galaxies is flux limited, sources which would lie below the detection threshold in the absence of lensing might be detected, provided the magnification is sufficient. This magnification bias differs from other selection effects in that it actually increases the number of observed lenses. The extent of the effect depends on the number of unlensed sources as a function of magnitude, at each redshift. For lensing of quasars, where the luminosity function is steep, magnification bias is a significant effect (Kochanek 1995). Keeton (1998) found that this was particularly important for the NFW profile, which produces higher mean magnifications than the singular isothermal sphere.

The key question is whether or not a particular lens survey is flux limited. Unlike quasars, galaxies in the Hubble Deep Field are spatially resolved, so a surface brightness threshold might be a better detection criterion. Since lensing does not change surface brightness, such a survey would have no magnification bias.

On the other hand, some aspects of lens surveys might impose a flux limit implicitly. For instance, the smaller the image flux, the harder it would be to obtain a spectrum of sufficient quality to confirm or rule out lensing. Zepf et al. (1997) used the flux of the faintest component of their three candidates systems to estimate an effective magnitude limit of $AB(8140) = 27$. With only eight components between these three systems, they do not attempt to prove that their sample is flux limited. However, that seems to be their assumption. Finally, as discussed in §2.3, Fernández-Soto et al. (1999) smooth the HDF images and use an isophotal magnitude limit so as not to exclude low surface brightness

galaxies. While this does not directly affect the lensing searches, it is another possible argument in favor of a flux limit. Nevertheless, it is difficult to decide whether the lens searches are better described by a flux limit or by a surface brightness limit.

To calculate the magnification bias for a flux limited lens survey, we would need to know the joint distribution with respect to magnitude and redshift of sources several magnitudes fainter than the effective magnitude limit of the survey. However, the photometric redshifts from the Hubble Deep Field are the deepest redshift survey available, extending to $AB(8140)$ of 28. We could impose a cut on the lens survey, eliminating candidates with magnitudes too close to 28, but this would further reduce the already small number of observed lens systems. Alternatively, we could extrapolate the observed magnitude-redshift distribution to fainter limits. Since magnitude and redshift are correlated, the already relatively small redshift catalog would have to be divided into redshift bands. Great care would be required to ensure that the extrapolation was not dominated by noise due to small number statistics and redshift clustering in the redshift catalog. In addition, any such extrapolation beyond the data carries an unknown risk of systematic error.

Considering these difficulties, we make the simpler choice of assuming a surface brightness limited sample for lensed galaxies searches in the HDF. We therefore neglect the effect of magnification bias on the expected number of lensed galaxies detected.

Even so, we might be concerned about magnification bias because of the explicit magnitude cut in the Fernández-Soto et al. (1999) redshift catalog. However, the effect on the number of galaxies observed is not the same as the effect on the number of lensed galaxies observed. The lens magnification reduces the effective luminosity limit of the flux-limited sample, but at the same time decreases the surface number density of sources. Broadhurst, Taylor, & Peacock (1995) pointed out that the observed number of galaxies N per unit solid angle is

$$N_0 \mu^{\beta(z)-1} \quad (21)$$

where N_0 is the number in the absence of lensing, μ is the local magnification, and $\beta(z)$ is minus the logarithmic derivative, $d \log n(L, z) / d \log L$, of the Galaxy luminosity function, $n(L, z)$, with respect to luminosity. The slope β depends of course on the source population. It is possible to select source populations of red galaxies for which β differs from unity, but for the faint blue galaxies which dominate the source population at high redshifts, β is found empirically to be very close to 1 (Broadhurst 1995; Taylor et al. 1998). For such galaxies, the two effects of magnification cancel, purely by coincidence. Thus the redshift distribution is unaffected by lensing.

3. RESULTS

In Table 1, we show the total number of lensed galaxies expected. Groups with singular isothermal sphere profiles produce roughly 200 times as many lensed galaxies as those with NFW profiles. Even for the SIS lenses, the expected number of lensed galaxies is $\lesssim 1$.

To understand the results, and to make predictions for future surveys, we show the distribution of lensed galaxies with respect to various properties of the lens and source. In Figure 3 we show the expected number distribution of lensed galaxies per unit logarithmic interval in the lens mass.

In Figure 4, we show the distribution of lenses with respect to redshift for NFW and SIS groups. The NFW lens distributions peak near z_l of 0.5–0.7 and are strongly suppressed at $z_l \lesssim 0.2$. Compared to the NFW results for the corresponding cosmology, each SIS lens distribution peaks at a redshift lower by ~ 0.2 , and shows only linear suppression at low redshifts. The difference at small redshifts reflects the lower lensing efficiency of the less singular NFW profile when the critical density, Σ_{cr} , is small (Keeton 1998). Given sufficient statistics (and constraints on the cosmology), the difference in lens redshift distributions is a potential discriminant between NFW and SIS lenses.

Figure 5 shows the redshift distributions of the lensed galaxies in the SCDM case. For comparison, the distribution in the NFW case has been multiplied by 200, so that it has the same total area as in the SIS case. The other three cosmologies have very similar distributions, apart from the normalization. Figure 5 reflects the discrete nature of our catalog-based source redshift distribution. The distribution of lensed galaxies in the NFW case is more strongly suppressed at low source redshift, again reflecting the lower lensing efficiency of the NFW profile when Σ_{cr} becomes small.

The probability distribution of angular separations between the two brightest images of lensed galaxies is shown in Figure 6. Most of the image separations are greater than $1''$, so there should be no difficulty in resolving the images even with ground-based observations.

Figure 7 shows the cumulative probability distribution, $p(> A)$, of lensed galaxies with total amplification greater than A . The much larger amplifications in the NFW case are consistent with the results of Keeton (1998).

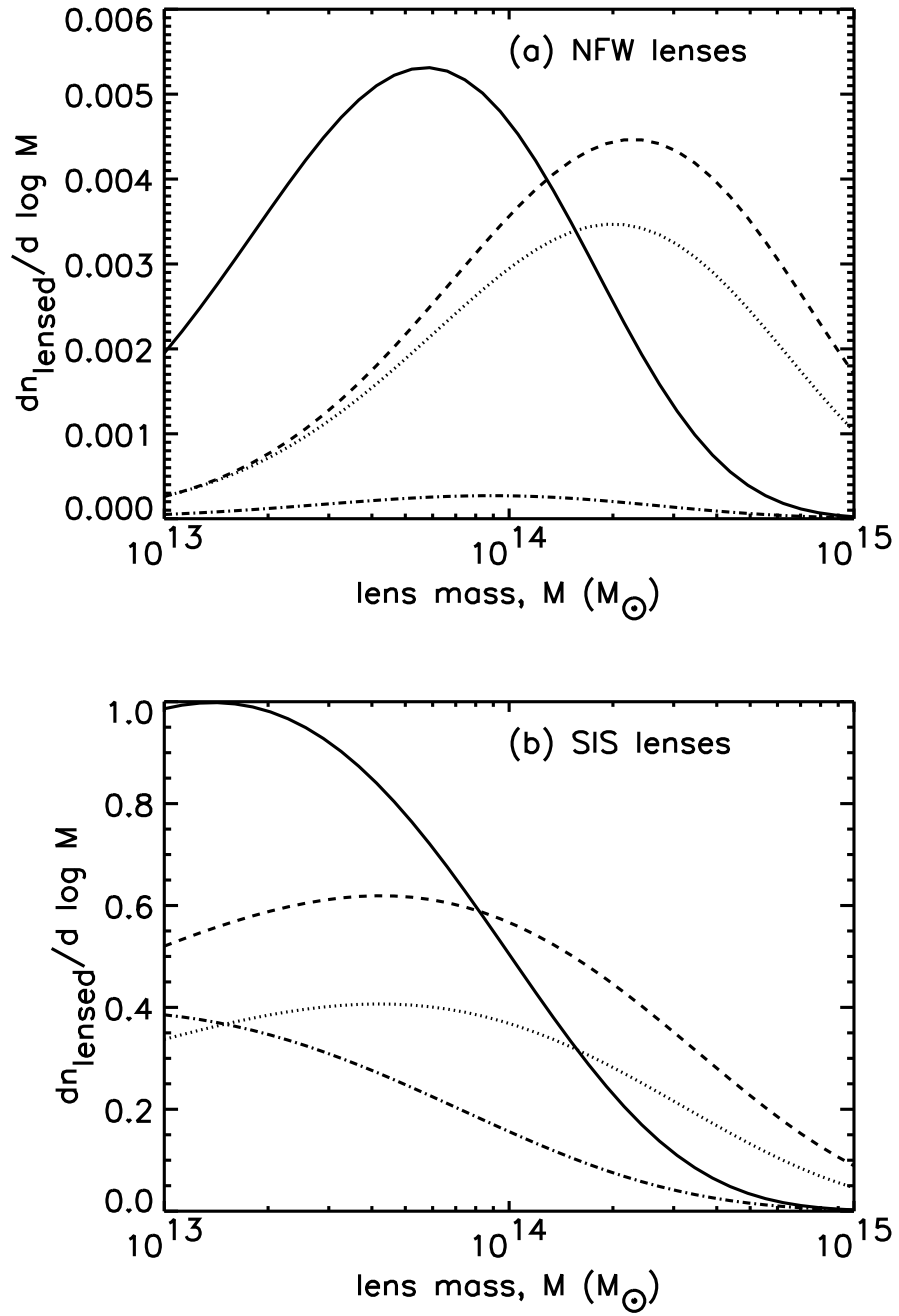


Fig. 3.— Number of lensed galaxies expected in the Hubble Deep Field per unit logarithmic interval in the lens mass, for groups with the (a) NFW profile and (b) SIS profile. The cosmologies are the same as in Figure 1.

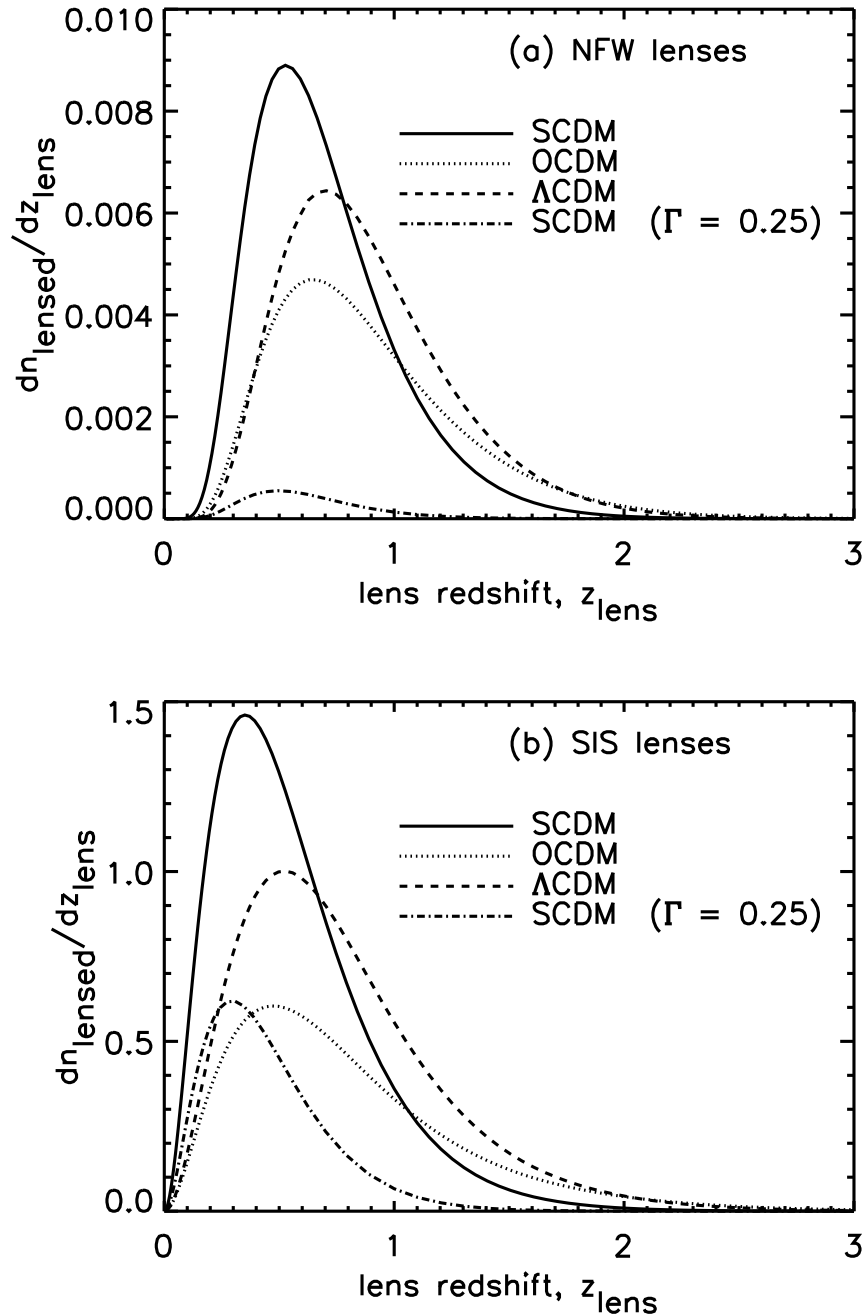


Fig. 4.— Number of lensed galaxies in the Hubble Deep Field per unit interval in lens redshift, for groups with the (a) NFW profile and (b) SIS profile, again for the same cosmologies as in Figure 1.

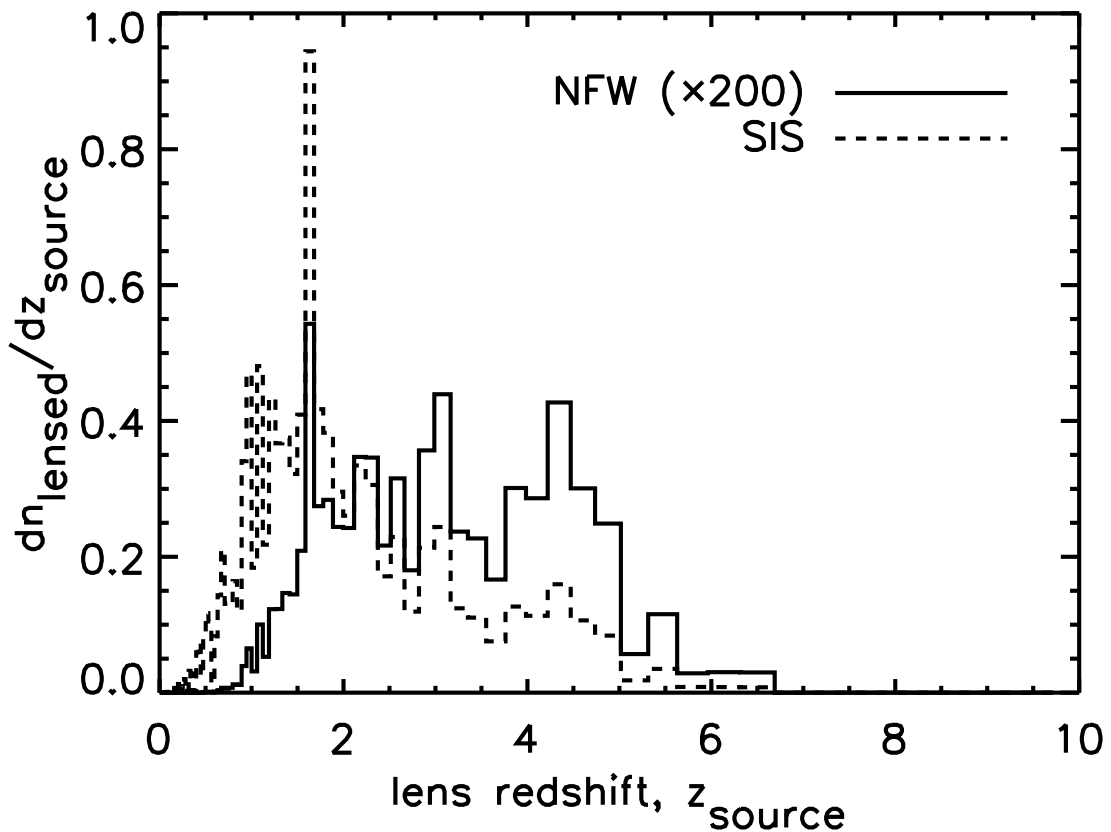


Fig. 5.— Number of lensed galaxies in the Hubble Deep Field per unit interval in redshift of the lensed galaxies themselves, for the SCDM case. Since the total number of lensed galaxies in the SIS case (dashed) is larger by a factor of 200, the distribution in the NFW case (solid) has been scaled up by a factor of 200 for comparison.

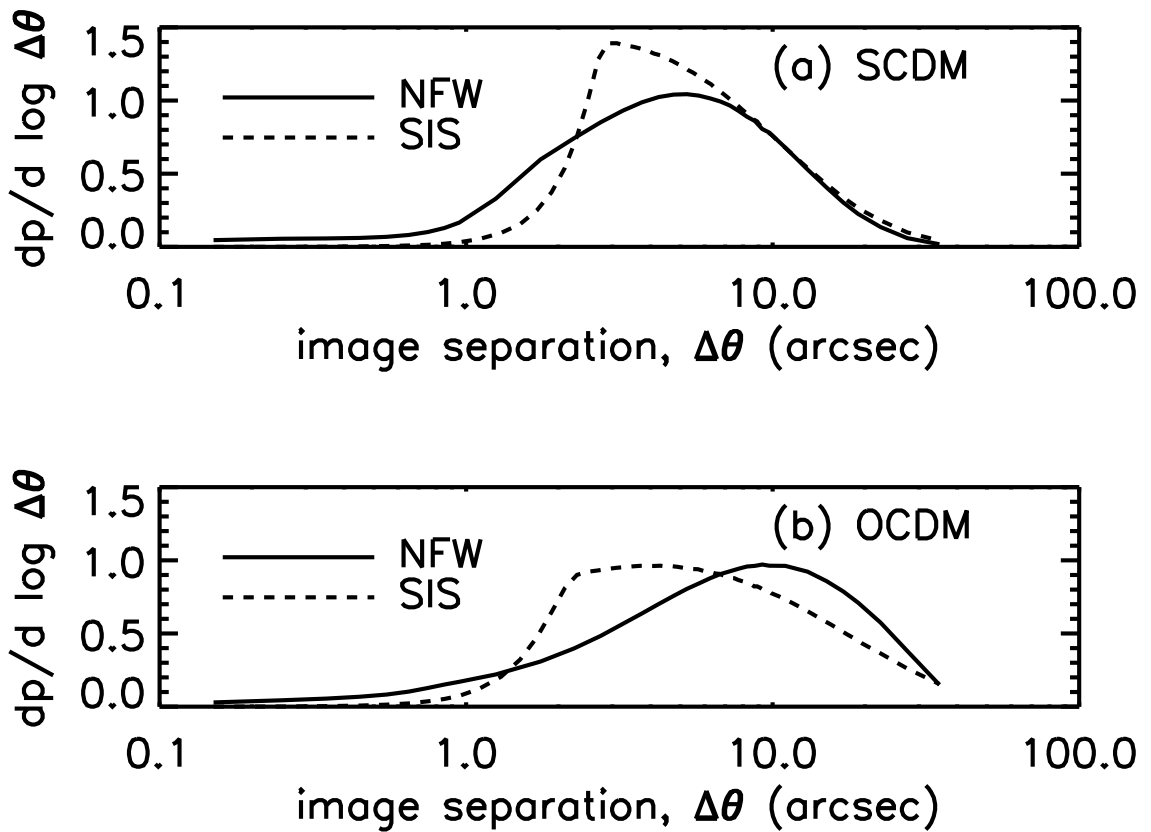


Fig. 6.— Probability distribution of image separations (between the two brightest images) in arcsec for sources lensed by NFW (solid) and SIS (dashed) halos, in (a) SCDM ($\Omega = 1$) and (b) OCDM ($\Omega = 0.3$). The low- Γ SCDM and Λ CDM results are similar to those for SCDM and OCDM, respectively.

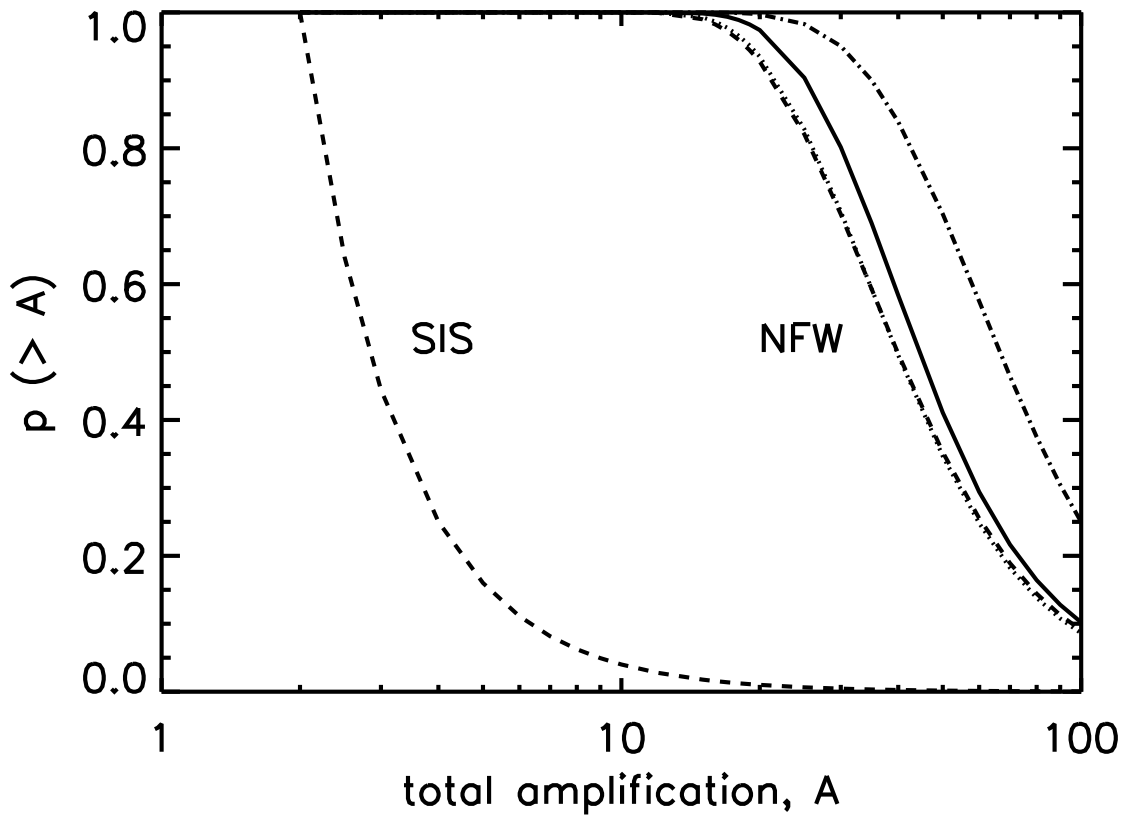


Fig. 7.— Cumulative probability distributions of lensed galaxies with respect to the minimum total amplification, for NFW lenses (the four curves at the right, with the same cosmologies as in Figure 1) and SIS lenses (the curve at the left. The amplification distribution of the SIS curve, $n(>A) = 4/A^2$, is independent of cosmology.

4. DISCUSSION

4.1. NFW vs. SIS

What makes the NFW profile so much less efficient at lensing than the singular isothermal sphere? Both the shape and the normalization of the profile matter. To see this, consider a specific example, a halo with mass $M_{\text{vir}} = 2 \times 10^{14} M_{\odot}$ at $z_l = 0.6$, typical of our NFW lenses, in an OCDM universe. Figure 8 compares the mean surface density, $\bar{\Sigma}(r) = M_{\text{cyl}}(r)/\pi r^2$, within a cylinder of radius r for NFW and SIS halos of this mass and redshift. Both have the same mass within the sphere of radius $r_{\text{vir}} \approx 1.0$ Mpc. However, the SIS profile has a larger mean surface density both at small radii ($\lesssim 80$ kpc) and at large radii ($\gtrsim 450$ kpc).

At large radii, this is due to the more rapid ($\rho \propto r^{-3}$) falloff of the NFW density profile. At small radii, the situation is more complicated. Our typical NFW lens has a scale radius, r_s , of 0.15 Mpc. For $r \ll r_s$, the NFW profile has a mean surface density

$$\bar{\Sigma}_{\text{NFW}}(r) \approx 2\rho_s r_s \ln r_s/r. \quad (22)$$

For fixed density, $\rho(r) = \rho_s r_s/r$, at small radii, $\bar{\Sigma}$ still depends, albeit logarithmically, on the scale radius. This occurs because, for density profiles $\rho(r)$ which are sufficiently shallow at small radii, $\rho(r)$ at intermediate radii $r \lesssim r_s$ can still contribute significantly to $\bar{\Sigma}(r)$ at radii $r \ll r_s$. For a profile with $\rho \propto r^{-p}$ at $r \ll r_s$ and $\rho \propto r^{-3}$ at $r \gg r_s$, and $1 < p < 2$, the ratio between the contribution to $\bar{\Sigma}(r)$ from intermediate radii and the contribution from small radii is roughly $(1/p)(r/r_s)^{p-1}$. As p approaches 1, there will still be a fractional contribution of $O(\epsilon)$ as long as $r/r_s \gtrsim \epsilon^{1/(p-1)}$.

Thus, the lower mean surface density of the NFW profile at small radii is due to the less rapid ($\rho \propto r^{-1}$) divergence of the NFW profile, but is also influenced by the falloff at large radii.

The key question is which portion of $\bar{\Sigma}(r)$ determines the multiple imaging cross section. The caustic radius, η_c , is determined only by the surface mass distribution within the radial critical curve. Locating the radial critical curve, $\xi = \xi_r$, requires solving the lens equation (19) for $d\eta/d\xi = 0$. This occurs where

$$\Sigma_{\text{cr}} = \frac{d}{d\xi} (\xi \bar{\Sigma}) \Big|_{\xi_r} = \bar{\Sigma} + \xi \frac{d\bar{\Sigma}}{d\xi} \Big|_{\xi_r}. \quad (23)$$

As long as the surface density decreases with radius, ξ_r is always inside the Einstein ring radius, r_E , defined by $\bar{\Sigma}(r_E) \equiv \Sigma_{\text{cr}}$. For a background galaxy at $z_s = 3$, the value of the critical surface density, Σ_{cr} , is shown as a horizontal line in Figure 8, which intersects $\bar{\Sigma}(r)$

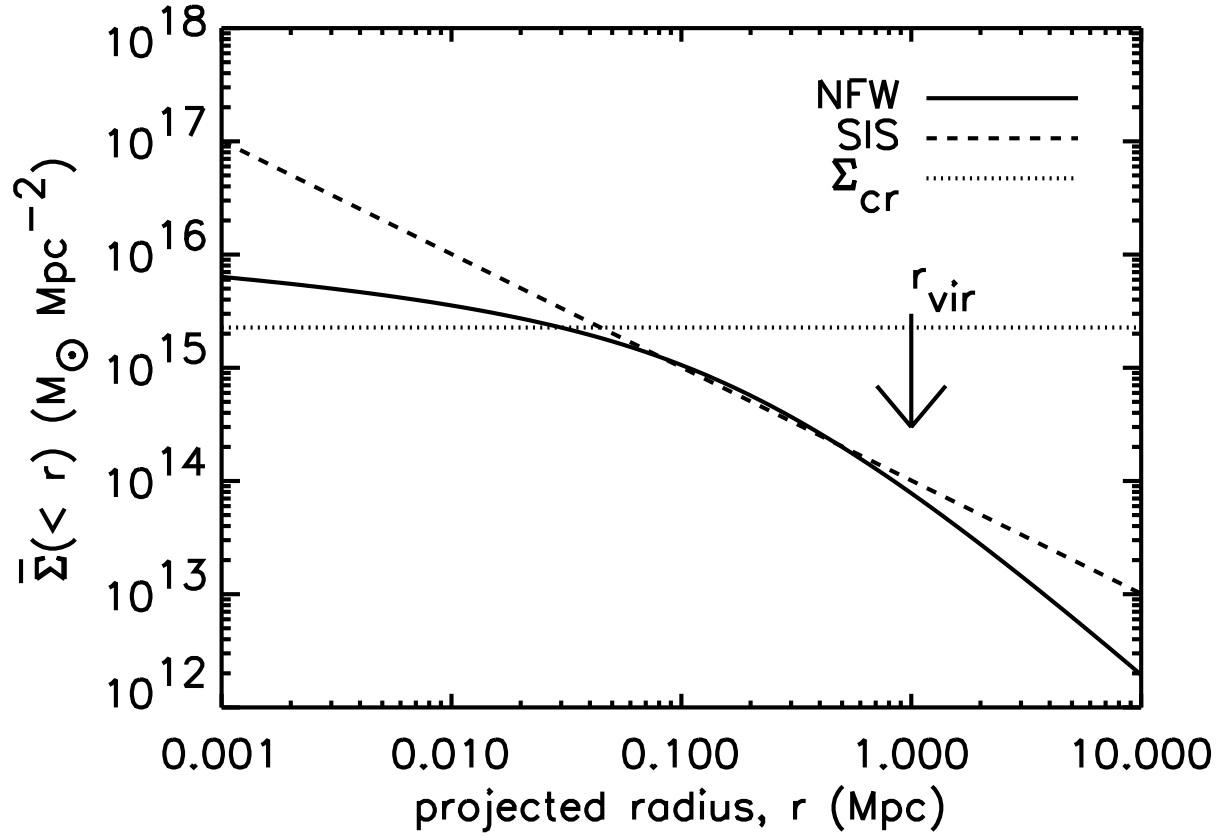


Fig. 8.— Mean surface density, $\bar{\Sigma}(r)$ within a radius r , for NFW (solid) and SIS (dashed) profiles of the same mass, $M = 2 \times 10^{14} M_\odot$, and redshift, $z_l = 0.6$, chosen to be typical of the NFW lenses, in an OCDM cosmology. The dotted horizontal line shows the critical surface density, Σ_{cr} , assuming a source redshift $z_s = 3$. It intersects each profile at its Einstein ring radius. The arrow indicates the location of the virial radius.

for the NFW profile at $r = 30$ kpc. At all points inside this radius, $\bar{\Sigma}$ is smaller for the NFW profile than the singular isothermal sphere.

To see how this difference in $\bar{\Sigma}(r)$ in the lens plane affects the cross section in the source plane, we need to refer back to the lens equation (19). It is useful to define the offset

$$\Delta(\xi) \equiv \left| \eta - \frac{D_s}{D_l} \xi \right| = \frac{D_s}{D_l} \left| \frac{\xi \bar{\Sigma}(\xi)}{\Sigma_{\text{cr}}} \right| \quad (24)$$

between the source and image positions (projected into the source plane). For the SIS profile, $\bar{\Sigma}(\xi) \propto 1/|\xi|$, so $\Delta(\xi)$ is independent of ξ .

For positive ξ , we can solve equation (24) for ξ and rewrite the lens equation as

$$\eta = -\Delta(\xi) (\Sigma_{\text{cr}} - \bar{\Sigma}(\xi)) / \bar{\Sigma}(\xi). \quad (25)$$

Evaluating this at the radial critical curve, using equation (23), we find

$$|\eta_c| = \Delta(\xi) \left. \frac{d \log \bar{\Sigma}}{d \log \xi} \right|_{\xi=\xi_r}. \quad (26)$$

For the SIS profile, this simplifies to $|\eta_c| = \Delta_{\text{SIS}}$. For our typical NFW profile, since $\xi_r < r_E$, and $r_E/r_s \approx 0.2$, we can use equation (22) for $\bar{\Sigma}$, to find

$$|\eta_c(\text{NFW})| = \Delta(\xi_r) / \ln(\xi_0/\xi_r) < \Delta(\xi_r). \quad (27)$$

Since Δ_{SIS} is constant, we can compare it to Δ_{NFW} at the critical radius for the NFW lens. The multiple lensing cross section is $\pi \eta_c^2$, so

$$\sigma_{\text{NFW}}/\sigma_{\text{SIS}} = \left[\frac{1}{\ln(\xi_0/\xi)} \frac{\bar{\Sigma}_{\text{NFW}}(\xi)}{\bar{\Sigma}_{\text{SIS}}(\xi)} \right]^2 \Bigg|_{\xi=\xi_r(\text{NFW})}. \quad (28)$$

Thus, the smaller cross section for the NFW lens is caused by the smaller mean surface density, $\bar{\Sigma}$, as well as by the smaller proportionality constant between η_c and $\Delta(\xi_r)$.

The dimensional lens equation (19) is shown in Figure 2 for the particular lens parameters above. The range of source positions for which there are multiple images for the NFW profile is just over one-eighth of that for the SIS profile, and thus the ratio of lensing cross sections, $\sigma_{\text{NFW}}/\sigma_{\text{SIS}}$, is $\lesssim 2\%$, in agreement with equation (28).

How do these results depend on mass? In Figure 9, we show the two cross sections as a function of mass, again for $z_l = 0.6$ and $z_s = 3.0$. The NFW cross section increases roughly as $M^{2.25}$ for this choice of redshifts, whereas the SIS cross section increases as $M^{4/3}$,

so $\sigma_{\text{NFW}}/\sigma_{\text{SIS}}$ increases with mass. This trend is evident in Figure 3. For the SIS profile, the increase in σ with mass is roughly offset by the decrease in the number of groups, so the distribution of lens masses is relatively flat or slightly declining between 10^{13} and $10^{14} M_{\odot}$. Because the NFW cross section depends more strongly on lens mass than the SIS cross section, its distribution increases with mass, peaking near $2 \times 10^{14} M_{\odot}$. The low efficiency of the NFW lenses at small masses, where halos are most abundant, further reduces the number of lensed galaxies. Even for a cluster with $10^{15} M_{\odot}$, $\sigma_{\text{NFW}}/\sigma_{\text{SIS}}$ is still only $\sim 5\%$, and such clusters are sufficiently rare in the Press-Schechter model that they contribute little to the optical depth for lensing. Our calculated $\sigma_{\text{NFW}}/\sigma_{\text{SIS}}$ ratios agree with those of Keeton (1998).

Given that the highest resolution simulations favor central profiles $\rho \propto r^{-p}$ with slope $p \approx 1.5$, it is interesting to ask how the cross section depends on p for $1 < p < 2$. Unfortunately, this is not a simple question to answer. As we have seen for the NFW lens, the multiple imaging cross section depends not only on the shape of the mean surface density profile, $\bar{\Sigma}(r)$, but on its normalization at small radii. For halos normalized to the same virial mass, fixing $\bar{\Sigma}(r)$ at small radii requires both p and the concentration $c_{\text{vir}} \equiv r_{\text{vir}}/r_s$, which determines how $\rho(r)$ turns over from r^{-p} at small radii to r^{-3} at large radii. For the NFW profile, the relationship of r_s to virial mass has been investigated extensively through simulations of many halos (Navarro et al. 1996, 1997). Bullock et al. (2000) have also investigated this relationship, and have found consistent results at $z = 0$, but lower mean concentrations at high redshift. The higher resolution simulations of Moore et al. (1998, 1999), who find a density profile of

$$\rho(r) \propto \frac{1}{(r/r_s)^{3/2} \left[1 + (r/r_s)^{3/2} \right]}, \quad (29)$$

require more computing time, and therefore have been done for only a few halos, so the dependence of the concentration, c_{vir} , on the virial mass has not been investigated systematically. Moore et al. (1999) do quote a value of $c_{\text{vir}} = 4$ for a single cluster with virial mass $4.3 \times 10^{14} M_{\odot}$ at $z = 0$ in a Standard CDM simulation. The multiple imaging cross section for a halo of that mass and concentration, but at $z = 0.6$ in our OCDM cosmology, is shown by the asterisk in Figure 8. This cross section is 4 times greater than the corresponding NFW profile, but still 7.6 times smaller than the SIS profile. If, as for an NFW cluster of the same mass, the concentration declines by 20% from $z = 0$ to $z = 0.6$, the cross section would be reduced by 45%, as shown by the plus sign in Figure 8. Because of the differences in cosmology and redshift, these comparisons offer at best a rough idea of the multiple imaging cross section for profiles with inner slopes intermediate between the NFW profile and a singular isothermal sphere. More precise quantitative predictions would require further high-resolution simulations to determine the variation of the concentration with halo mass

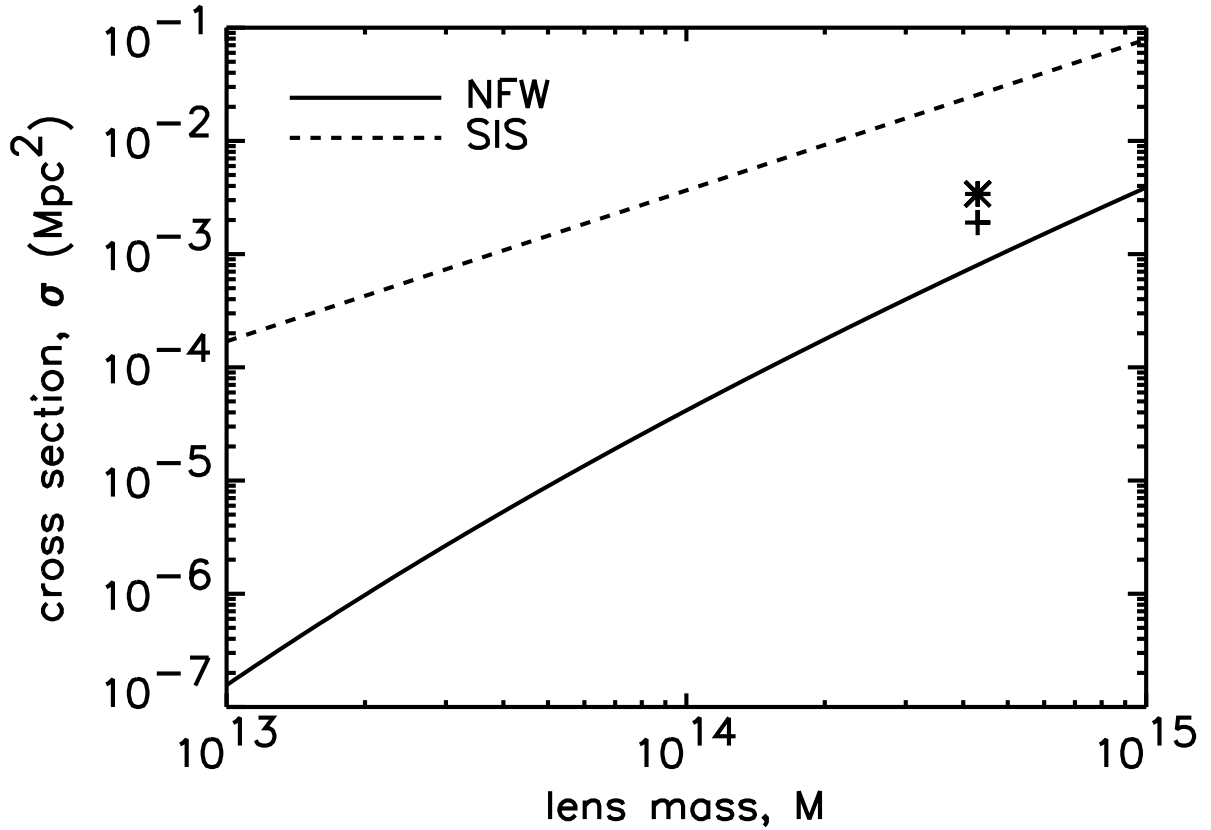


Fig. 9.— Multiple lensing cross sections as a function of mass for the NFW (solid) and singular isothermal sphere (dashed) profiles, with lens redshift $z_l = 0.6$ and source redshift $z_s = 3.0$ in an OCDM cosmology. The asterisk indicates the cross section for a cluster described by equation (29), from the simulations of Moore et al. (1999), with $M_{\text{vir}} = 4.3 \times 10^{14} M_\odot$ and $c_{\text{vir}} \equiv r_{\text{vir}}/r_s = 4$. The plus sign indicates the cross section for a cluster of the same mass, with the concentration reduced by 20% in a rough attempt to estimate the scaling between the $z = 0$ simulation and the assumed lens redshift of 0.6

and redshift.

4.2. Cosmology Dependence

Consider the distribution of NFW lens masses shown in Figure 3. The distributions for Open CDM (dotted) and Λ CDM (dashed) are quite similar up to normalization. The Λ CDM case has about 35% more lenses, due to the larger path length and greater angular diameter distance to a given redshift. The shape of these distributions reflects the competition between the increase in σ with mass, and the decreasing abundance of halos. At low masses, the rapid increase in the NFW lensing cross section with mass dominates, and the distributions rise until $\sim 2\text{--}3 \times 10^{14} M_\odot$, where they are truncated by the high-end cutoff in the mass function (see Figure 1).

Given that Standard CDM has the smallest path length and angular diameter distances of the three models, we expect it to have the fewest lenses. Surprisingly, our calculations indicate slightly more total lensed galaxies in the SCDM case than in the Λ CDM case (see Table 1 and Figure 3). The reason can be seen in Figure 1. Compared to the Λ CDM and OCDM cases, the SCDM mass function cuts off at a lower mass due to the lower value of σ_8 . Its lens mass distribution therefore peaks at a lower mass $\sim 6 \times 10^{13} M_\odot$. However, the SCDM mass function also has a steeper slope, due to a larger value of Ω_0 and thus Γ_{eff} , resulting in a *larger* number of groups on smaller mass scales (by a factor of ≈ 3 for $M = 10^{13} M_\odot$ and $z = 0.6$) when the power spectrum is normalized to σ_8 . To verify this explanation, we have included a low- Γ CDM model with $\Omega = 1$ and σ_8 still equal to 0.53, but with $\Gamma = 0.25$. The low- Γ model (dot-dashed), barely visible at the bottom of Figure 3, does indeed have far fewer lenses than the other cosmological models.

Our low mass cutoff at $10^{13} M_\odot$ does have an effect on the total number of lensed galaxies in the SIS case. Extending the mass function down to $10^{12} M_\odot$ would increase the number of SIS lenses expected by a factor of 2 for $\Omega = 1$ and of 1.4 for $\Omega = 0.3$. By contrast, this change would increase the number of NFW lenses by only 10 percent for SCDM, with a smaller effect for the other cosmologies.

The difference between our two $\Omega = 1$ models highlights the sensitivity of predicted lensing by groups to the value of the shape parameter, Γ , as previously noted by Kochanek (1995). With the power spectrum normalization fixed by the cluster temperature function, increasing Γ produces significantly more groups. Eke et al. (1996) note that the normalization of the cluster temperature function constrains σ_8 well, since the co-moving radius $R = 8 h^{-1} \text{Mpc}$ is close to the cluster scale, but that the slope of the temperature function, and

thus Γ , is not well determined. Measurements of the galaxy correlation function favor $\Gamma \approx 0.25$ (Maddox, Efstathiou, & Sutherland 1996) as does the cluster mass function inferred from the group luminosity function and an assumed constant mass-to-light ratio (Bahcall & Cen 1993).

As an aside, we note that the Bahcall & Cen (1993) mass function has a similar shape to our Press-Schechter distribution in the OCDM case, but 40% more low mass groups at $z = 0$. However, the Press-Schechter mass function evolves significantly between $z = 0$ and $z = 0.6$ where our lens redshift distribution peaks, whereas the Bahcall & Cen (1993) mass function, inferred from low z observations, contains no redshift evolution information. As an experiment, we have repeated our calculation using the Bahcall & Cen (1993) mass function and simply ignoring evolution. In the OCDM case, with NFW lenses, this yields 20 times as many lensed galaxies as the Press-Schechter mass function, rather than 1.4 times as many, greatly exaggerating the number of lensed galaxies expected. A realistic calculation of lensing using a group mass function determined observationally at low z would require the addition of evolution information.

Turning things around, lensing may be able to constrain the group mass function and thus Γ . Kochanek (1995) finds that values of Γ between 0.15 and 0.30 are also needed to reconcile large separation quasar lensing statistics with the COBE normalization of σ_8 in an SCDM universe. To constrain Γ with lensing of galaxies by groups, we would need enough lensed galaxies to detect this effect and disentangle it from the effects of other unknown parameters. The small total number of strong lenses expected in the HDF prevents us from making such inferences.

5. CONCLUSIONS

Groups and clusters with the NFW profile are far less efficient at producing lensed galaxies than singular isothermal spheres of the same mass. The ratio, $\sigma_{\text{NFW}}/\sigma_{\text{SIS}}$, of multiple imaging cross sections ranges from 7×10^{-4} for a $10^{13} M_\odot$ group to 5×10^{-2} for a $10^{15} M_\odot$ cluster. The lower efficiency of NFW lenses is a result of their smaller surface density profile, $\bar{\Sigma}(r)$, for radii much smaller than the scale radius, r_s . This, in turn, is due to the shallower density profile, $\rho(r)$, at small radii (although it also depends logarithmically on r_s , which determines the more rapid falloff in density at large radii). In principle, this makes the statistics of multiple imaging a sensitive test of the central density profile of groups.

Unfortunately, the number of galaxies in the Hubble Deep Field is not sufficient to perform such a test. Lensing by SIS groups might be detected with a sample a few times

larger. However, to detect NFW groups would require more than 200 times as many galaxies. No deep space-based survey of this size is expected in the near future. Ground-based surveys would be limited to much lower redshift sources, and would therefore suffer from smaller optical depths for multiple imaging. Still, they might compensate with sufficiently larger fields containing many more galaxies. For example the Sloan Digital Sky Survey (SDSS) is expected to obtain photometry for 5×10^7 galaxies, as compared to 10^3 in the Hubble Deep Field.

On the other hand, lensing searches in the HDF illustrate the difficulties of finding lensed galaxies. Two of the three candidates systems identified by morphology and colors were subsequently ruled out by spectroscopy. In both cases, hypothetical multiple images turned out to be different galaxies. Such a high rate of false positives limits the number of true lens systems which can be identified in a given amount of spectroscopic follow-up time. It is unclear whether the different galaxies were physically associated or not. In either case, false positives due to chance superposition are more likely at the larger image separations expected for lensing by groups. In contrast, with lensed quasars, coincidences are negligible, although pairs of physically associated quasars are still an issue (Kochanek, Falco, & Muñoz 1999). Furthermore, the high luminosity and prominent spectral features of quasars simplify spectroscopic confirmation. The SDSS is also expected to yield a large sample of quasars, which may be a more promising way of detecting lensing by groups.

Finally, weak lensing statistics may complement strong lensing by probing the outer portions of the mass profiles of groups. A number of detections of weak lensing by galaxies (Brainerd, Blandford, & Smail 1996; Dell'Antonio & Tyson 1996; Hudson et al. 1998; Fischer et al. 1999) and even one early detection of weak lensing by groups (e.g., Hoekstra, Franx, & Kuijken 1999) have been reported. We will discuss the detection and analysis of weak lensing by groups in a subsequent paper.

We thank Abraham Loeb for suggesting this project and for his advice on the work. We thank William Forman, Irwin Shapiro, and Lars Hernquist for their advice and support, and for their comments on the paper drafts, which substantially improved the final result. We also thank the anonymous referee, whose suggestions improved the discussion of the sensitivity of the cross section to the halo profile. This work was supported by NASA GSRP Fellowship NGT5-50028 for D. C. F and NSERC Grant 72013704 for U.-L. P. One of the authors (D. C. F.) would like to acknowledge Dragon Systems, Inc., whose DragonDictate for Windows and Dragon NaturallySpeaking software were essential to the development of the code for this calculation and to the preparation of the paper.

REFERENCES

Bahcall, N. A., & Cen, R. 1993, *ApJ*, 407, L49

Bardeen, J. M., Bond, J. R., Kaiser, N., & Szalay, A. S. 1986, *ApJ*, 304, 15

Barkana, R. & Loeb, A. 2000, *ApJ*, 531, 613

Bartelmann, M. 1996, *A&A*, 313, 697

Brainerd, T. G., Blandford, R. D., & Smail, I. 1996, *ApJ*, 466, 623

Brainerd, T. G., Goldberg, D. M., & Villumsen, J. V. 1998, *ApJ*, 502, 505

Broadhurst, T. J. 1995 in *AIP Conf. Proc.* 336, Dark Matter, ed. S. S. Holt & C. L. Bennett (New York: AIP)

Broadhurst, T. J., Taylor, A. N., & Peacock, J. A. 1995, *ApJ*, 438, 49

Bullock, J. S. et al. 1999, *MNRAS*, submitted (astro-ph/9908159)

Burkert, A. 1995, *ApJ*, 447, L25

Burkert, A. & Silk, J. 1997, *ApJ*, 488, L55

Burles, S. & Tytler, D. 1998, *ApJ*, 507, 732

Carlberg, R. G., et al. 1997, *ApJ*, 485, L13

Carroll, S. M., Press, W. H., & Turner, E. L. 1992, *ARA&A*, 30, 499

Cole, S., & Lacey, C. 1996, *MNRAS*, 281, 716

Cooray, A. R. 1999, *A&A*, 341, 653

Cooray, A. R., Quashnock, J. M., & Miller, M. C. 1999, *ApJ*, 511, 562

Dell'Antonio, I. P., & Tyson, J. A. 1996, *ApJ*, 473, L17

Dickinson, M., et al. 1998, in preparation

Dubinski, J., & Carlberg, R. G. 1991, *ApJ*, 378, 496

Eke, V. R., Cole, S., & Frenk, C. S. 1996, *MNRAS*, 282, 263

Fernández-Soto, A., Lanzetta, K. M., & Yahil, A. 1999, *ApJ*, 513, 34

Fischer, P., et al. 1999, AJ, submitted (astro-ph/9912119)

Flores, R. A., & Primack, J. R. 1994, ApJ, 427, L1

Flores, R. A., & Primack, J. R. 1996, ApJ, 457, L5

Fukugita, M., Ichikawa, T., Gunn, J. E., Doi, M., Shimasaku, K., & Schneider, D. P. 1996, AJ, 111, 1748

Fukushige, T., & Makino, J. 1997, ApJ, 477, 9

Gelato, S., & Sommer-Larsen, J. 1999, MNRAS, 303, 321

Hernquist, L. 1990, ApJ, 356, 359

Hoekstra, H., Franx, M., & Kuijken, K. 1999, to appear in Gravitational Lensing: Recent Progress and Future Goals ASP conference series, eds. T. Brainerd & C. S. Kochanek (astro-ph/9911106)

Hogg, D. W., Blandford, R., Kundić, T., Fassnacht, C. D., & Malhotra, S. 1996, ApJ, 467, 73

Hogg, D. W., et al. 1998, AJ, 115, 1418

Hudson, M. J., Gwyn, D. J., Dahle, H., & Kaiser, N. 1998, ApJ, 503, 531

Keeton, C. R. 1998, doctoral thesis (Harvard University)

Kneib, J.-P., Ellis, R. S., Smail, I., Couch, W. J., & Sharples, R. M. 1996, ApJ, 471, 643

Kochanek, C. S. 1995, ApJ, 453, 545

Kochanek, C. S., Falco, E. E., & Muñoz, J. A. 1999, ApJ, 510, 590

Kravtsov, A. V., Klypin, A. A., Bullock, J. S., & Primack, J. R. 1998, ApJ, 502, 48

Lacey, C. & Cole, S. 1993, MNRAS, 262, 627

Lanzetta, K. M., Yahil, A., & Fernández-Soto, A. 1996, Nature, 381, 759

Mahdavi, A., Geller, M. J., Böhringer, H., Kurtz, M. J., & Ramella, M. 1999, ApJ, 518, 69

Maoz, D., Rix, H.-W., Gal-Yam, A., & Gould, A. 1997, ApJ, 486, 75

Markevitch, M., Vikhlinin, A., Forman, W. R., & Sarazin, C. L. 1999, ApJ, 527, 545

Maddox, S. J., Efstathiou, G., & Sutherland, W. J. 1996, MNRAS, 283, 1227

Moore, B. 1994, Nature, 370, 629

Moore, B., Governato, F., Quinn, T., Stadel, J., & Lake, G. 1999, ApJ, 499, L5

Moore, B., Quinn, T., Governato, F., Stadel, J., & Lake, G. 1999, MNRAS, 310, 1147

Myers, S. T., et al. 1995, ApJ, 447, L5

Narayan, R. & White, S. D. M. 1988, MNRAS, 231, P97

Navarro, J. F., Eke, V. R., & Frenk, C. S. 1996, MNRAS, 283, L72

Navarro, J. F., Frenk, C. S., & White, S. D. M. 1995, MNRAS, 275, 720

Navarro, J. F., Frenk, C. S., & White, S. D. M. 1996, ApJ, 462, 563

Navarro, J. F., Frenk, C. S., & White, S. D. M. 1997, ApJ, 490, 493

Nevalainen, J., Markevitch, M., & Forman, W. 1999, ApJ, 526, 1

Pen, U. 1998, ApJ, 498, 60

Press, W. H. & Schechter, P. 1974, ApJ431, L71

Sawicki, M. J., Lin, H., & Yee, H. K. C. 1997, AJ, 113, 1

Schneider, P., Ehlers, J., & Falco, E. 1992, Gravitational Lenses (Berlin: Springer-Verlag)

Taylor, A. N., Dye, S., Broadhurst, T. J., Benítez, N., & van Kampen, E. 1998, ApJ, 501, 539

Tormen, G., Bouchet, F. R., & White, S. D. M. 1997, MNRAS, 286, 865

Wang, Y., Bahcall, R., & Turner, E. L. 1998, AJ, 116, 2081

Williams, L. L. R., Navarro, J. F., & Bartelmann, M. 1999, ApJ, 527, 535

Williams, R. E., et al. 1996, AJ, 112, 1335

Zepf, S. E., Moustakas, L. A., & Davis, M. 1997, ApJ, 474, 1

Table 1: Expected Number of Lensed Galaxies in the HDF

lens type	cosmology	number of lenses expected
NFW	SCDM	5.9×10^{-3}
	OCDM	4.1×10^{-3}
	Λ CDM	5.2×10^{-3}
	SCDM (low Γ)	3.1×10^{-4}
SIS	SCDM	1.0×10^0
	OCDM	6.0×10^{-1}
	Λ CDM	9.3×10^{-1}
	SCDM (low Γ)	3.5×10^{-1}